Bulletin of the Seismological Society of America, Vol. 88, No. 6, pp. 1548–1560, December 1998

# Near-Surface Scattering Effects Observed with a High-Frequency Phased Array at Pinyon Flats, California

by Frank L. Vernon, Gary L. Pavlis, Tom J. Owens, Dan E. McNamara, and Paul N. Anderson

**Abstract** Analysis of data collected by a high-frequency array experiment conducted at Pinyon Flat in southern California provides strong evidence that the high-frequency wave field from local earthquakes at this hard-rock site are strongly distorted by near-surface scattering. The seismic array we deployed consisted of 60, 2-Hz natural frequency, three-component sensors deployed in a three-dimensional array. Two of the sensors were located in boreholes at 150 and 275 m depth. The other 58 sensors were deployed in an areal array above these boreholes. Thirty-six of these were deployed in a 6-by-6 element grid array with a nominal spacing of 7 m centered over the borehole sensors. The remaining 22 seismometers were laid out in two 11-element linear arrays radiating outward from the grid. Coherence calculations reveal a rapid loss of coherence at frequencies over 15 Hz at all but the shortest length scales of this array. Three-dimensional visualization techniques were used to closely examine the spatial stability of particle motions of *P* and *S* waves. This reveals systematic variations of particle motion across the array in which the particle motion tracks tilt drastically away from the backazimuth expected for an isotropic medium. These variations, however, are frequency dependent. Below around 8 Hz, the particle motions become virtually identical for all stations. At progressively higher frequencies, the wave-field particle motion becomes increasingly chaotic. Frequency-wavenumber analysis of these data provide quantitative measures of the same phenomena. We find that direct wave *f-k* spectra are bathed in a background of signal-generated noise that varies from 10 to 30 dB down from the direct arrival signal. This signal-generated noise appears to be nearly white in wavenumber indicating the wavelength of this "noise" on the scale of tens of meters and less. Refraction measurements we made on two lines crisscrossing the array reveal that the weathered layer velocities are highly variable and define a very strong wave guide. Measured surface *P*-wave velocities varied from 400 to 1300 m/sec, and velocities at depth of approximately 15 m varied from 1600 to 2700 m/sec. Previous measurements in the boreholes showed that the intact granite below about 65 m depth has a velocity of approximately 5400 m/sec. These results demonstrate the extreme velocity contrast and degree of velocity heterogeneity of the near surface at this site. We conclude that all the observations we made can be explained by strong scattering of incident body-wave signals into a complex mishmash of body-wave and surface-wave modes in this heterogeneous near-surface wave guide.

## Introduction

The basic data of seismology are ground motion recorded in the form of the wiggly lines we call seismograms. Tremendous advances have been achieved in the past decade in modeling waveforms of major global phases recorded at regional and teleseismic distances (e.g., Dziewonski *et al.,* 1981; Holt and Wallace, 1987; Fan and Wallace, 1991; Song and Helmberger, 1992; Helmberger *et al.,* 1993). Although we still have a long way to go in explaining all the complexities in modern, broadband seismograms, long-period seismograms are routinely modeled to remarkable precision for stations anywhere in the world. In marked contrast, however, understanding high-frequency seismograms written by local earthquakes has proven much more difficult. Hundreds of thousands of local earthquake seismograms are recorded

in digital form in this country every year at a cost of millions of dollars, but almost all of these data are used only to measure *P* and *S* phase arrival times. A major reason for this fact is that all current networks have stations spaced no closer than approximately 10 km, and almost all stations are equipped with sensors having natural frequency no lower than 1 Hz. Teleseismic waveforms, in contrast, rarely contain much signal at frequencies higher than 1 Hz due to attenuation. This basic observation suggests something fundamental is happening to complicate seismic waveforms at frequencies somewhere above 1 Hz. The results of this article support strongly a hypothesis that this major complicating factor is heterogeneity in the near-surface weathered layer.

The puzzle of why high-frequency seismograms are so complicated has a long history. The real landmark work that led to the earliest recognition of the problem appears to have grown out of an early series of array experiments in the early 1960s. These so-called Geneva or Berkner arrays were deployed at that time to lower the detection threshold of underground nuclear tests (Carpenter, 1965; Filson, 1975). Results from these early experiments are now an integral part of the foundation of modern seismology, although a considerable amount of important technical detail from this era is buried in assorted government reports (see, e.g., Green *et al.,* 1965; Davies, 1973; Filson, 1975; and references therein). Nonetheless, these early array experiments yielded some fundamentally important new data. It is a tribute to those involved that results from the Geneva arrays were synthesized very quickly and used to design one of the landmark experiments in modern seismology that was dubbed the large aperture seismic array (LASA).

The LASA was a remarkable success. It accomplished its primary objective of using array processing techniques to significantly lower the detection threshold of earthquakes and explosions worldwide. Nevertheless, results from the LASA also revealed a serious problem. That is, in spite of the fact that all the short-period sensors were deployed in 61- or 152-m-deep boreholes and that the LASA data were comparatively narrow band by modern standards (1 to 5 Hz) (Forbes *et al.,* 1965), major deviations in waveforms and amplitudes were observed across LASA (e.g., Capon *et al.,* 1968). The individual elements had station spacings between 0.5 and 7 km in each subarray. Since then, a significant amount of data has accumulated to demonstrate that there is considerable variation in the seismic wave field on very short distance scales (e.g., McLaughlin *et al.,* 1983; King and Tucker, 1984; Menke *et al.,* 1991). In 1985, a nine-element array with a 500-m aperture and a 50-m minimum spacing was deployed at the Pinyon Flat Observatory in California (Vernon *et al,* 1991). They found that, even for a site with optimal topographical characteristics and uniform geology, the seismic wave field is distorted substantially over the observable distances.

This article presents first-order results from a 60-element, three-dimensional, high-frequency array experiment we deployed at Pinyon Flat, California, in the spring of 1990. The most unique aspect of this experiment was the extremely close spacing of sensors within the array. Thirty-six of the elements were located within a 35- by 35-m area that fits completely inside the inner ring used in the 1985 experiment. This allows us to analyze features of the seismic wave fields produced by earthquake sources at distance scales of at least an order of magnitude smaller than any previous array experiment. Our results demonstrate a remarkable amount of variability in waveforms observed at this scale.

## Geologic Setting

The choice of Pinyon Flat as the site for this experiment was made to resolve questions from results of the first small aperture array experiment on Pinyon Flat (Vernon *et al.,* 1991). Pinyon Flat is located entirely on the Santa Rosa Mountain pluton (Dibblee, 1981) in the northernmost part of the Peninsular Ranges batholith in southern California. The array was located at the Pinyon Flat Observatory (PFO) (Fig. 1) on a nearly planar surface centered 730 m N47°W from the center of the previous experiment. The general near-surface geological and seismic properties of Pinyon Flat have been discussed previously (Wyatt, 1982, 1989;

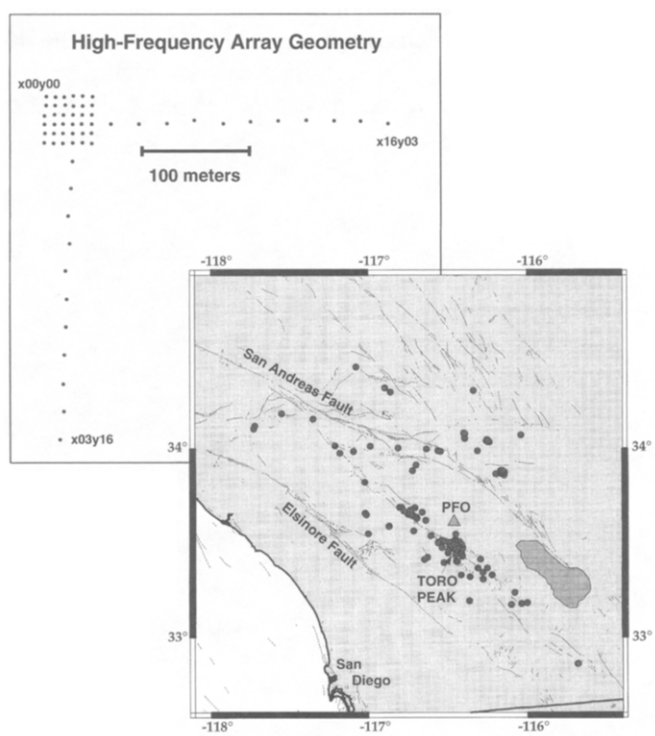


Figure 1. High-frequency array geometry is shown in the upper left plot. Stations within the grid have a 7-m separation from the next nearest sensor, and sensors along the E–W and N–S arms have a spacing of 21 m. The lower right plot contains the map showing location of the array in southern California and the epicenters of the recorded events.

Fletcher *et al.,* 1990; Vernon *et al.,* 1991). The surface layer is almost totally decomposed granite that approaches the consistency of sand. This grades into grus, corestones, and finally jointed granite by a depth of approximately 25 m. Seismic velocity models for the PFO site are monotonically increasing with depth with velocities at the surface of 0.34 and 0.156 km/sec and at 160 m depth velocities of 5.4 and 3.0 km/sec for *P* and *S* waves, respectively.

## Experimental Data

A surface array of 58 Mark Products L-22 2-Hz three-component seismometers was collocated with a USGS borehole experiment (Fletcher *et al.,* 1990) where L-22 seismometers were installed at 150 and 275 m depth. The surface array was deployed with a 36-element grid and two extended arms each with 11 elements (Fig. 1). The sensor spacing was nominally 7 m in the grid and 21 m along the arms. Each surface sensor was plastered to semi-competent rock at the bottom of a pit that had been dug with a backhoe. We properly label the material at the bottom of these pits semi-competent because as Wyatt (1982, 1989) points out, this is not intact rock, but the top of the partially weathered grus layer. The pit depths, depending on where each point of refusal was found, ranged between 1 and 3 m. Figure 2 gives an indication of the variability in depth for the decomposed granite weathering layer.

The data were recorded on 30 PASSCAL REFTEK RT72A-02 dataloggers. Each six-channel datalogger recorded two elements of the array at 250 samples/second. The array was operated in a master and slave configuration with the signals from the two borehole sensors being connected to the master datalogger. When the trigger algorithm in the master detected an event, a signal was sent through a special distribution box to simultaneously trigger all the surface slave units. Each RT72A-02 also received a common time signal from a True Time OMEGA clock through the previously mentioned distribution box. This allowed all data channels to be synchronously sampled. Each trigger produced 90 sec of data for each channel with 15-sec pre-event memory. For further technical details about the experiment, please refer to Owens *et al.* (1991).

The Pinyon Flat, high-frequency array was operated between 18 April and 27 May 1990. During this time, 324 events were recorded and a subset of 138 events were associated with events in the Southern California Seismic Network or ANZA network catalogs. Figure 1 shows the distribution of events recorded by this array. Epicentral distances ranged from 6 to 240 km and depths ranged from 0 to 20 km. The largest event recorded had a magnitude of 4.2. About half of the earthquake sources were located due south near the array in a cluster of events located under Toro Peak.

## Velocity Measurements

At the conclusion of the experiment, we conducted a shallow refraction experiment to investigate the structure of the weathered layer at Pinyon. This refraction experiment was conducted using a 12-channel, stacking recorder with a hand-operated thumper source. Each shot point was stacked

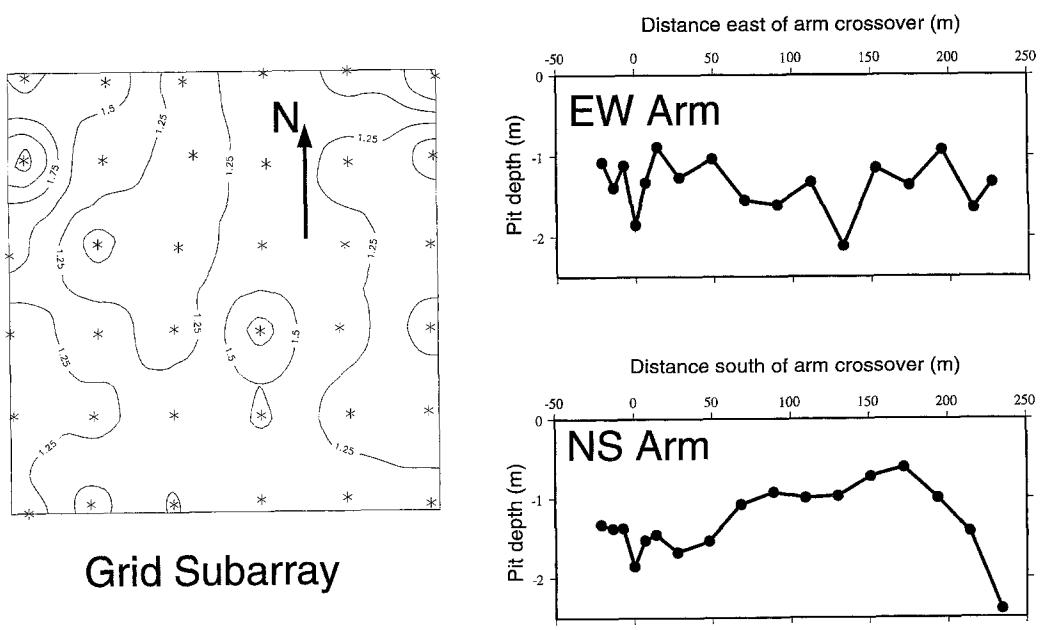


Figure 2. Depths of seismometer emplacements. Each seismometer pit was dug to the point of refusal using a backhoe. The depths for the grid subarray are shown on the contour plot, and the depths for the N–S and E–W arms are plotted as a function distance from the mutual crossover point. The depths vary between 1.0 and 2.5 m.

with from 50 to 100 pops depending upon background noise levels. Two lines were shot. A north–south line was shot from the grid to the end of the south arm. An east–west line was shot with the identical geometry from the grid to the end of the east arm of the array. Both lines used a shooting geometry best thought of as reversed CDP shooting. That is, we shot two sets of off-end CDP lines with shots at three station (21 m) intervals: one with the active cable ahead of the shot point, and the reverse line with the cable trailing the shot point. This produced 10 reversed refraction spreads on each line with mid-points positioned at 21-m intervals. The shot points were positioned so that the source was in one of the sensor pits (21-m spacing along the arms). The only exceptions were the two shot points on each end of each line that were positioned off the ends of the array.

The shallow refraction profiles shot along the arms of the array provide important baseline data that bears on our inference that the signals recorded by the passive array are dominated by near-surface scattering. Previous work by Wyatt (1982) indicated the presence of an extreme low-velocity weathered layer at PFO with surface velocities of 0.5 km/sec rising to 2 km/sec by at least 18 m in depth. Furthermore, sonic logs of the boreholes that contained the borehole sensors we used for this experiment indicate compressional velocities of 4 km/s at 65 m depths, rising to over 5 km/sec by 80 m (Fletcher *et al.,* 1990).

We present the results of travel-time measurements from the data we shot in Figures 3 and 4. These results present two complimentary views of the weathered layer at Pinyon. Figure 3 gives velocities measured from first arrivals at the geophone nearest the shot point. In all cases shown, the source was offset 7 m from the nearest geophone, and for most of these, the source was located in the shallow pits that had been dug earlier for the high-frequency array. The velocities shown are calculated by simply dividing the total source-receiver distance (i.e., including shot depth) by the measured travel time. The results from these measurements demonstrate two things. First, the upper meter or so of the soil at Pinyon has an extremely slow velocity. The average of the measured velocities in Figure 3 is only 0.63 km/sec with a standard deviation of 0.18 km/sec. The velocity of sound in air is only 0.330 km/sec, so the measured velocities of the dry sand that forms the soil at Pinyon is not that different from air. The second feature to note about the near offset velocity measurements is that the measured soil velocities vary consistently with position. Both lines show a slight decrease in soil velocities in the positive direction (south for the N–S line and east for the E–W line). The N–S line, however, has five points that show significantly higher velocities. We suspect this is a result of the fact that the soil layer is noticeably thinner (less than 1 m) directly south of the grid stations (Fig. 2), and these higher velocities may be the result of less weathered rock at these points.

The second result we wish to present is based on the 10 reversed profiles from each line. Figure 4 shows the measured refractor velocities from each spread calculated using

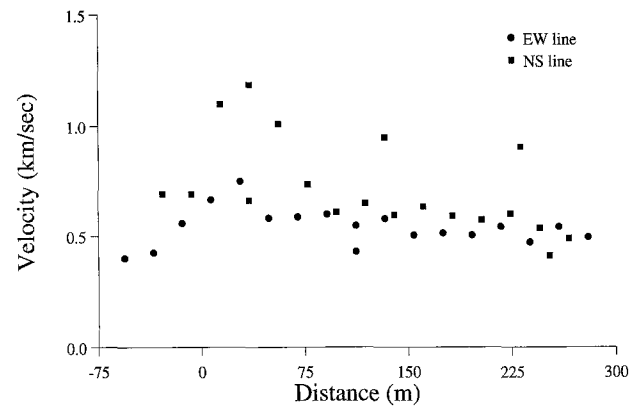


Figure 3. Near-offset velocities measured from shallow refraction data. Velocities shown are calculated from measured travel times from the shot point to the closest sensor. In all cases shown, this was a 7-m offset plus a depth correction for shots located in sensor pits. Measured velocities are plotted here as a function of distance from the intersection of the profiles, which is defined here by the intersection of lines drawn through the two arms of the array (Fig. 1). For the N–S line, positive distances are south, and for the E–W line, positive distances are to the east.

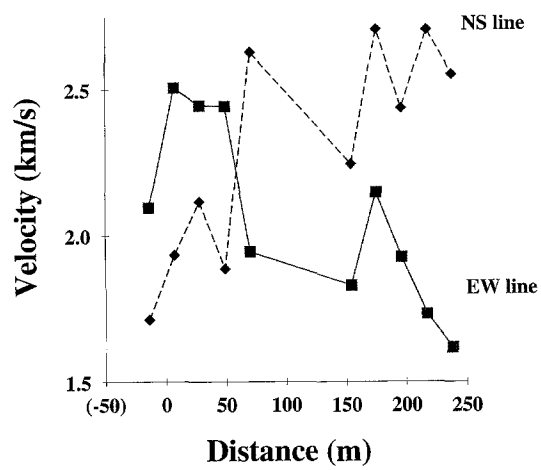


Figure 4. Refraction velocities measured from shallow refraction data using the plus–minus method. The distance scale is as described in the caption of Figure 2.

the plus–minus method (Hagedoorn, 1959; Cummings, 1979) with least-squares line fits of the minus terms. The plus–minus method is based on an assumption that each measured travel time can be expressed as

$$t_{ij} = \tau_i + \tau_j + X_{ij}/v,$$

where $t_{ij}$ is the measured travel time from source $i$ to receiver $j$, $\tau_i$ and $\tau_j$ are delay times for shot and receiver, $X_{ij}$ is the distance between shot and receiver, and $v$ is the refractor

velocity that is assumed to be constant. This approximation is reasonable for shallow refraction experiments like this where offsets are very short (largest offset here is 84 m) (Cummings, 1979), although it is clearly not perfect here because most travel-time curves constructed from these data show a prominent convex down form characteristic of a strong velocity gradient in the near surface. However, our objective here was to consider lateral changes in the upper layer velocities, and for this purpose, the shooting arrangement we used and interpretation with the plus–minus method is a reasonable choice.

We note the following features of the refractor velocities we calculated with the plus–minus method.

1. The results of the velocity measurements are internally consistent. That is, we see two first-order trends in the data. On the north–south profile, velocity increases to the south, whereas for the east–west profile, the tendency is for the velocity to decrease to the east. These results are consistent with field observations of soil profiles in the pits. That is, the pits along the southern arm of the array were all less than 1 m deep (except the two southernmost stations), indicating a shallower weathered layer (Fig. 2). Similarly, on the east arm, the pits were all consistently much deeper and the rock was clearly more deeply weathered than that seen along pits along the south arm.
2. The measured refractor velocities are extremely variable ranging from 1.6 to 2.7 km/sec. The refractor velocities have a mean of 2.18 km/sec and a standard deviation of 0.57 km/sec, which are consistent with rays bottoming at less than 15 m depth when compared to the results of Wyatt (1982) and Fletcher *et al.* (1990). Furthermore, the two orthogonal lines do not match where they cross at the 0 mark in Figure 4. That is, the measured velocities on the east–west line are considerably higher than the measured velocities at the same point on the north–south line. The difference, however, is well within the range of variation in other measurements, so we interpret this to indicate that the lines do not tie because the two profiles sample distinctly different blocks of weathered rock.

### Coherence Analysis

A natural starting point in presenting our results is to consider the average coherence properties of seismic body waves as a function of station spacing and frequency. Coherence for the vertical, radial, and transverse components were calculated for 2-sec windows centered on the *P* and *S* phases for every station pair for the event shown in Figure 5b. The technique used is described in detail in Vernon *et al.* (1991) and is based on the multiple taper method developed by Thomson (1982). For this analysis, we used a time-bandwidth product of 6.5 with 12 tapers. Because there were 58 surface elements with a minimum station spacing of 7 m and an aperture of 259 m [compared to the 9-element, 50-m minimum spacing and 500-m aperture array used in Vernon *et al.* (1991)], it was not necessary to use the cubic spline averaging across distance pairs that Vernon *et al.* (1991) were forced to use.

Figure 6 shows the results of this analysis applied to the *P* wave on the vertical components. Significant coherence at station spacings of 20 m occurs at frequencies as high as 100 Hz, but at the widest spacing observable with this array (240 m), coherence falls off rapidly above 20 Hz. High coherence (above 0.9) is found at 15 Hz at 20-m separation and at 5 Hz at 240-m separation. These results are consistent with Vernon *et al.* (1991) for intersensor distances between 50 and 240 m. Comparable results for *P* waves on the radial components (somewhat less coherent than for the verticals) and transverse (nearly incoherent) are also found between the present study and Vernon *et al.* (1991).

A comparison with the coherence between surface sensors at 245-m spacing to measurements between the 275-m borehole and the surface sensors is presented in Figure 7. The surface sensors become incoherent at frequencies above 20 Hz while the borehole-surface coherence shows significant coherence to above 40 Hz. This is a clear indication that the primary source of the signal distortion is occurring near to the surface. To verify this conclusion, we also show the coherence estimate between the two borehole instruments, at 275 and 150 m depth, finding that the coherence between these two sensors extends to nearly 60 Hz, which further supports the argument that near-surface effects cause the increased decoherence of the surface measurements.

## Particle Motions

The foregoing coherence results provide quantitative evidence that mother nature is doing something drastic at this site to distort the wave field on very short distance scales. A more striking demonstration of this fact is demonstrated by the use of graphical visualization techniques developed by Pavlis and Anderson (1990), Anderson (1993), and Repin and Pavlis (1997). They describe a technique for visualizing three-component seismic array data that is partially captured in Figure 8.

Figure 8 is best understood as a generalization of conventional particle motion plots. That is, we plot particle motion for each station in three dimensions for a specific time window. (Here, this is a window approximately 0.1-sec long beginning at the *P*-wave arrival time.) This three-dimensional object is then laid down in a three-dimensional space at a point scaled to the location of that station. The overall graphical object we are displaying in Figure 8 is then the composite of all these particle motion plots viewed in a 3D perspective plot. The view here is focused on the array grid. Individual stations can be seen, but note that stations X3Y5 and X2Y1 were unusable for this event and thus plot only as a dot. Figure 8 captures only a fraction of the information in the original display because this is only one frame of an animation display. In the original display, the individual par-

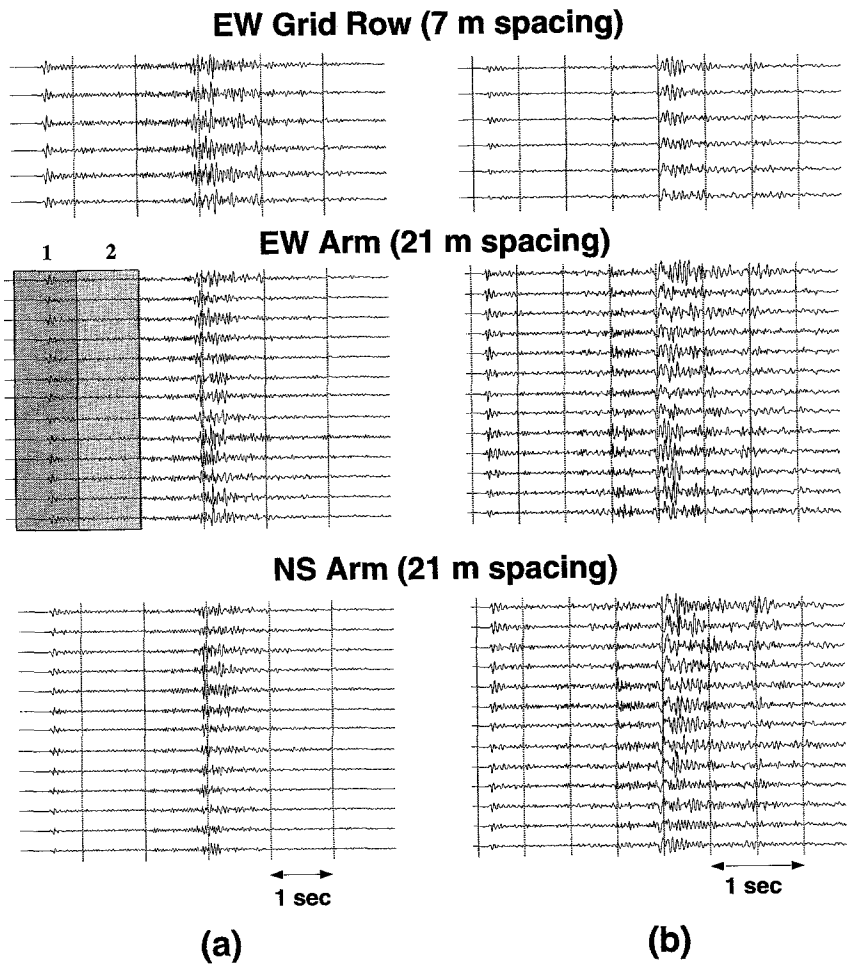


Figure 5. (a) Seismograms from selected vertical sensors for the 14 May 1990 05:05:27.1 GMT, $Ml = 1.8$, event with an epicentral distance of 16 km, depth of 11.8 km, station-event azimuth of 240°. The two numbered gray shaded boxes delineate two sections used for the *f-k* analysis on the vertical components. (b) Seismograms from selected vertical sensors for the 25 May 1990 03:59:23.6 GMT, $Ml = 1.8$, event with an epicentral distance of 11.7 km, depth of 7.88 km, station-event azimuth of 178°.

ticle tracks are constantly changing as the overall seismogram is traced out in time. This provides a broader perspective on these data than can be presented in the more limited static display shown in Figure 8, but for the purposes of this article, Figure 8 tells most of the story. We ask the reader to note the following:

1. Figure 8a displays the particle motion plots for the *P* wave of an $Ml = 2.6$ event located 16 km away at an azimuth of 240° that occurred on 14 May 1990 at 05:05:27.1 GMT (Fig. 5a). The view in Figure 8 is from directly west (30° clockwise from the propagation direction). Most of the particle motions are skewed from the theoretical azimuth for a *P* wave in a homogeneous medium, and the variations change smoothly across the array.
2. Because Figure 8 is only a projection, it does not tell the whole story. If this object is viewed from the north, one observes that the particle motions, in all cases, define elliptical orbits. The apparently linear particle motion is only a consequence of the view chosen here. The correct perspective is that the very first motion at each station is within a few degrees of the 240° backazimuth, but the motion very quickly gets distorted into this complex series of loops. This elliptical particle motion is almost certainly a direct consequence of interaction of the wave field with the weathered layer. Clear evidence for this is presented in Figure 9. There we display *P*-wave particle motion plots from the 150- and 275-m-deep borehole stations and compare them to a typical surface station. The borehole sensor outputs are almost perfectly linearly polarized, while all the surface sensors show elliptical particle motion. We suggest the most likely cause of this is complex scattering within the strongly heterogeneous weathered zone. *P*-to-*S* conversions on horizontal boundaries would be polarized purely in the radial-vertical plane and arrive slightly behind the direct *P* wave. Interference between the original *P* and this delayed *S* is the most likely explanation for the elliptical particle motions we see. The novel feature revealed by Figure 9 is that at Pinyon, the near-surface scattering is highly three dimensional. If we were dealing with a homogeneous weathered layer, we could still expect elliptical polarization, but we would expect all the stations to orbit in the same plane (the radial-vertical plane if the only source of scattering were *P-S* converted phases on a horizontal plane). Instead, Figures 8 and 9 show strong evidence for some type of three-dimensional scattering on the scale of this

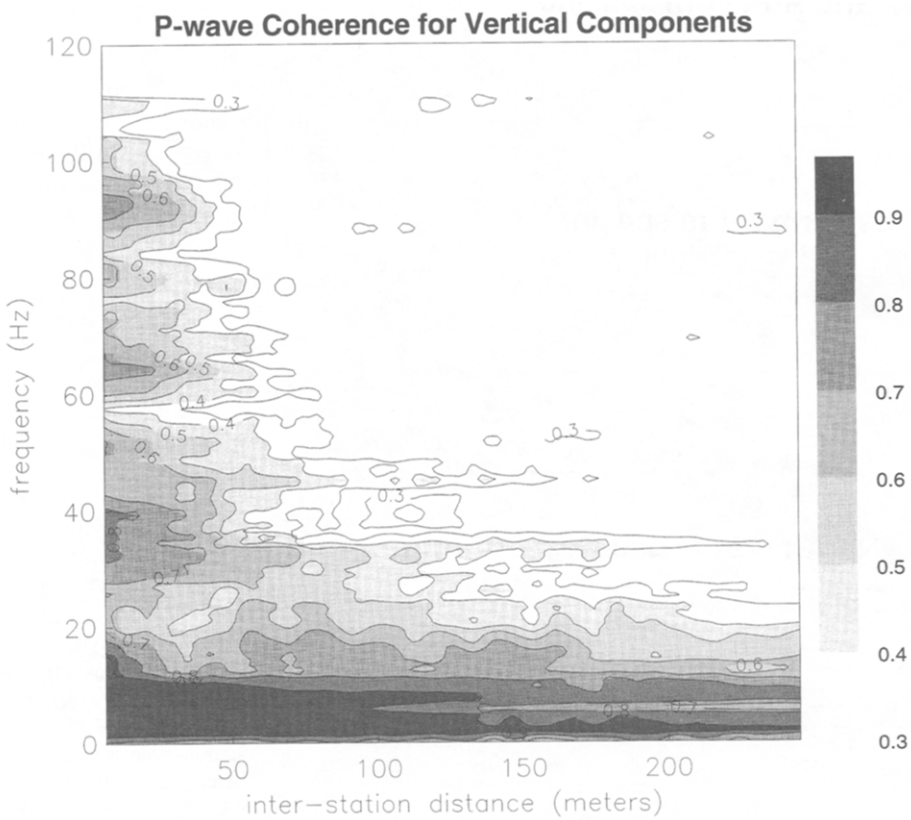


Figure 6. Contour plots of average magnitude-squared coherence for the vertical component of the *P* wave in Figure 5b plotted against distance and frequency. White signifies region where coherence has less than 95% confidence of being not equal to 0.

array. No layered model could produce the effects we see. We suggest that scattering in the near surface produces a complex mix of interfering modes. What we see in the particle motions is the interference effect of an unknown mix of *P*-to-*S* conversions, *P*-to-Rayleigh wave conversions, and scattered *P* modes.

3. This phenomenon is highly frequency dependent. Figure 8b shows the same data as Figure 8a but after low-pass filtering the data with a corner frequency of 8 Hz. The same systematic variations across the grid are seen as the unfiltered data in 8a, but the random background is missing. We note that we have not chosen to display the opposite of Figure 8b because it is not very informative. That is, if one does a high-pass filter at 10 Hz on these data, the particle motions are nearly random (Anderson, 1993). Finally, if one goes to lower frequencies, the picture is easily described in words: all particle motion tracks become identical. Eight Hertz seems to be close to a transitional boundary for this site. At higher frequencies, the wave field rapidly becomes chaotic. Just below this frequency, the particle motions all become identical. Note that this transition frequency is completely consistent with the coherence calculations discussed earlier.

## Frequency-Wavenumber Analysis

The linear arms of this array with approximately equally spaced sensors allow us to apply a technique commonly applied in the analysis of noise tests in seismic reflection processing that is usually referred to as *f-k* analysis. This numerical procedure centers around a two-dimensional discrete Fourier transform with one variable being time and the other being distance along the axis of a linear array (e.g., Lindseth, 1982). Because the sensors are approximately equally spaced, this can be accomplished using standard FFT algorithms. In particular, we used the *f-k* analysis modules in Sierraseis (trademark of Sierra Geophysics Inc.).

Some results of applying this analysis to the event shown in Figure 5a are presented in Figure 10. These figures show *f-k* power spectra calculated for three different time windows. All have the following fixed parameters:

1. All traces have been equalized to a standard 2-Hz geophone response using transfer functions calculated using calibration data for these sensors described by Menke *et al.* (1991).
2. The array arms each have 13 equally spaced stations. The Sierraseis FKPLOT algorithm rounds this to 16 and zero

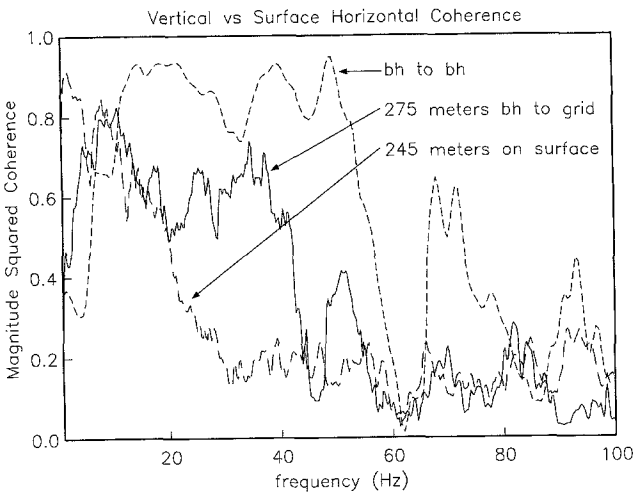


Figure 7. Comparison of average magnitude-squared coherence between vertical components for surface sensors located 245 m apart and between the 275-m borehole and surface grid sensors. The higher coherence as a function of frequency found between the borehole–surface sensors compared to surface–surface sensors indicates that the source of the scattering is in the near surface. Additionally, the comparison of the coherence between the two boreholes (at 275 and 150 m depth) show significant coherence to 60 Hz supporting the argument that the loss of coherence at lower frequencies is found near the surface.

pads the three dummy traces so inserted. The results shown thus have a grid that is defined by only 16 points along the $k$ axis.

3. All spectra were calculated using a 1-sec time window. This choice was based on the fact that the data were collected using 2-Hz sensors, so longer time windows were inappropriate.
4. The data were originally sampled at 250 samples/second. We do not plot data out to the Nyquist frequency in Figure 10 as the signal levels for the event analyzed there are small above 80 Hz.

Figure 10a shows the $f$-$k$ spectrum for a 1-sec window with the center of the window at the first arrival as seen on the east–west arm of the array with the vertical component. The seismograms that form this spectra can be seen in Figure 5a as the window from 0.0 to 1.0 sec. This spectrum is dominated by the first 0.5 sec of the $P$ waveform. The earthquake recorded here was almost due west of the array. We see the dominant energy corresponding to the $P$ wave with an apparent velocity of about 5 km/sec. However, we also see that even this early in the signal there are significant amounts of energy traveling at very low apparent velocities at a level about 20 dB down from the $P$-wave signal. Low apparent velocity signals become even more prevalent later in the signal. Figure 10b shows the $f$-$k$ spectrum in the $P$ coda for the 1-sec window immediately following that shown in Figure 10a (1.0- to 2.0-sec section of the seismograms in Fig. 5a. In this part of the signal, there is a diffuse band at all wavenumbers in the 10- to 35-Hz range with the central peak corresponding to $P$ waves scattered from more distant sources only about 10 dB above this diffuse background. Finally, Figure 10c shows the spectrum for a window centered on the $S$ wave as seen in the east–west component. This is essentially the radial component for this event. Here we see the same diffuse background in the 10- to 20-Hz band, but the prominent peak corresponding to the direct arrival dominates the spectrum again. (In this case, the direct wave is about 30 dB above the background.)

The background "noise" signal we are seeing in these data is not noise in the sense of a random background. Measurements of the $f$-$k$ spectra of the pre-event noise indicate the gains of the recording instruments were sufficiently low that the array was just barely resolving ground noise so that ground noise levels are only a few counts. Because the signals seen in Figure 5 have amplitudes of several thousand counts, the signal-to-noise ratio in these data is huge. Thus, the noise we are seeing in Figures 10a to 10c, which is dominated by the diffuse band of energy in the 10- to 35-Hz band spanning all wavenumbers, is signal-generated noise. We applied an $f$-$k$ filter to remove all energy from the signal with an apparent velocity higher than 2 km/sec. In this case, the $P$ wave virtually disappeared, and we were left with a nearly random background signal that turned on at about the $P$-wave arrival time and remained at an amplitude level of about 10% of the unfiltered signals. This suggests that the process generating the noise is scaled to the incoming wave field, which is additional evidence that the source of this noise is near-surface scattering.

## Discussion and Conclusions

We believe the results of this experiment demonstrate strongly that high-frequency seismograms recorded at Pinyon Flat are strongly contaminated by signal-generated noise, and this noise is dominated by near-surface scattering. We begin by summarizing several relevant observations previously presented.

1. The entire array sits on a nearly flat surface of weathered granite. Numerous observations indicate that the near surface in this area grades from soil into grus and then into intact granite. However, in spite of the fact that the top surface is nearly flat, the same is not true of the subsurface. The depth of weathering varies enormously varying from essentially zero on outcrops to 20 m or more over most of the area (Wyatt, 1982, 1989). Furthermore, it is most likely true that weathering occurs along major joints to much greater depths. Thus, the near-surface weathered layer can be thought of as having a flat top but a diffuse and highly irregular internal structure.
2. Refraction measurements (Wyatt, 1982; this study) show that the near-surface weathered layer is an extremely strong low-velocity zone. Measured soil velocities are

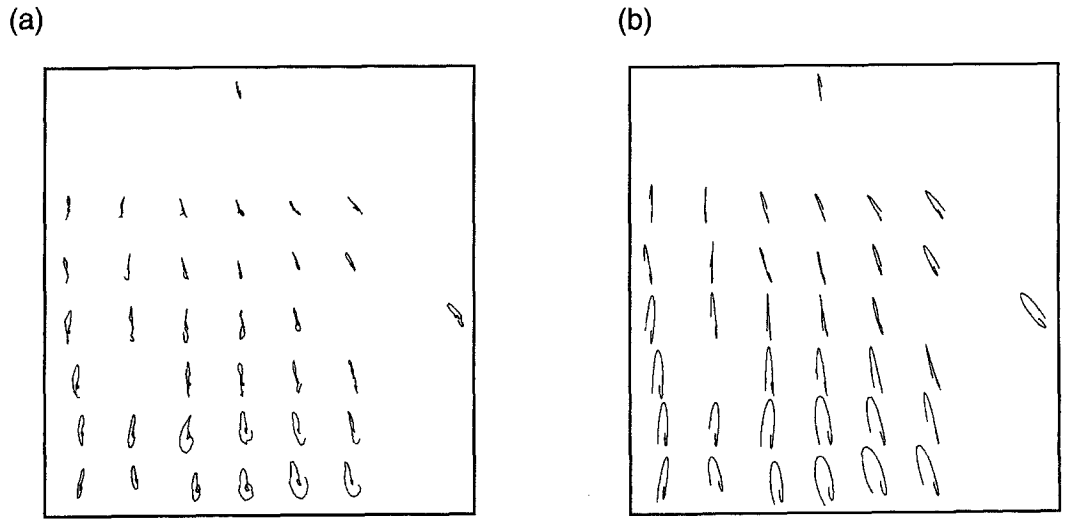


Figure 8. Three-dimensional perspective view of array particle motions. This figure is a snapshot from an animation display developed by Anderson (1993) that displays particle motions in three-dimensional perspective for the entire array. The particle motion tracks shown are for the first two cycles of the *P*-wave signal from the event in Figure 5a, and the view here is from due west and slightly above the array. The back-azimuth to the source is at 240°, or about 30° away from this viewpoint. Part (a) is a display of the unfiltered velocity output of the array sensors, and (b) is the same data low-pass filtered with a corner at 8 Hz. Note the systematic variations in the particle motion orientations seen in both figures. Further note that all these particle motion tracks are actually elliptical in shape. This is not seen here because we are looking in a direction down the axes of these elliptical figures.

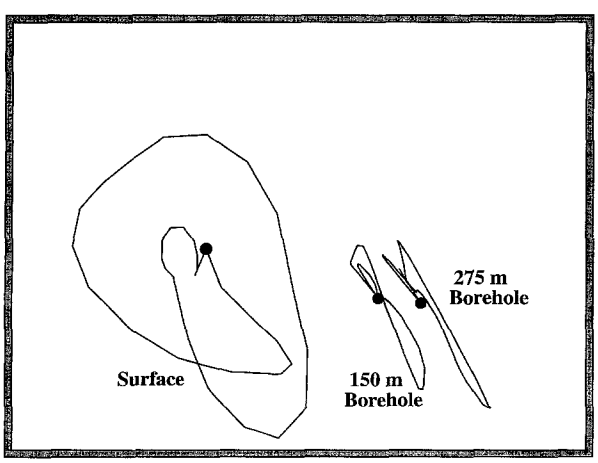


Figure 9. Comparison of surface and borehole sensors particle motions. The track for the surface sensors is for the first two cycles of the same *P*-wave signal seen in Figure 8a. The surface sensor shown is X0Y0, which is at the lower left corner of Figure 8a. The other two particle motion diagrams are for the same event but for the two borehole sensors. In all cases, the viewpoint is from the transverse direction. Note that the borehole sensors are linearly polarized while the surface sensors are all elliptically polarized.

only about 0.6 km/sec. Our refraction measurements show that the transition zone from soil to rock is highly variable with reversed profiles at different positions along the arms of the array showing velocities ranging from 1.6 to 2.7 km/sec. Borehole velocity log measurements, however, indicate that at the center of the array, intact granite is found at a depth of only about 15 m. This indicates that the weathered layer should serve as an extremely strong wave guide to trap any seismic energy that is scattered into it.

3. Waveform coherence calculations indicate a rapid fall-off of coherence as a function of distance along the surface. At distances of 245 m at the surface, compressional waves have significant coherence at frequencies less than 20 Hz. However, the coherence between a 275-m-deep borehole sensor and sensors in the surface grid show remarkably high coherence at frequencies up to 40 Hz. This is a strong indication that the variability of the surface observations of the seismic wave field are caused by variations in the very near-surface structure.
4. Visualization displays of the array data using computer animation (Pavlis *et al.,* 1990; Anderson, 1993) show strikingly how wildly signals observed from the three-

(a)

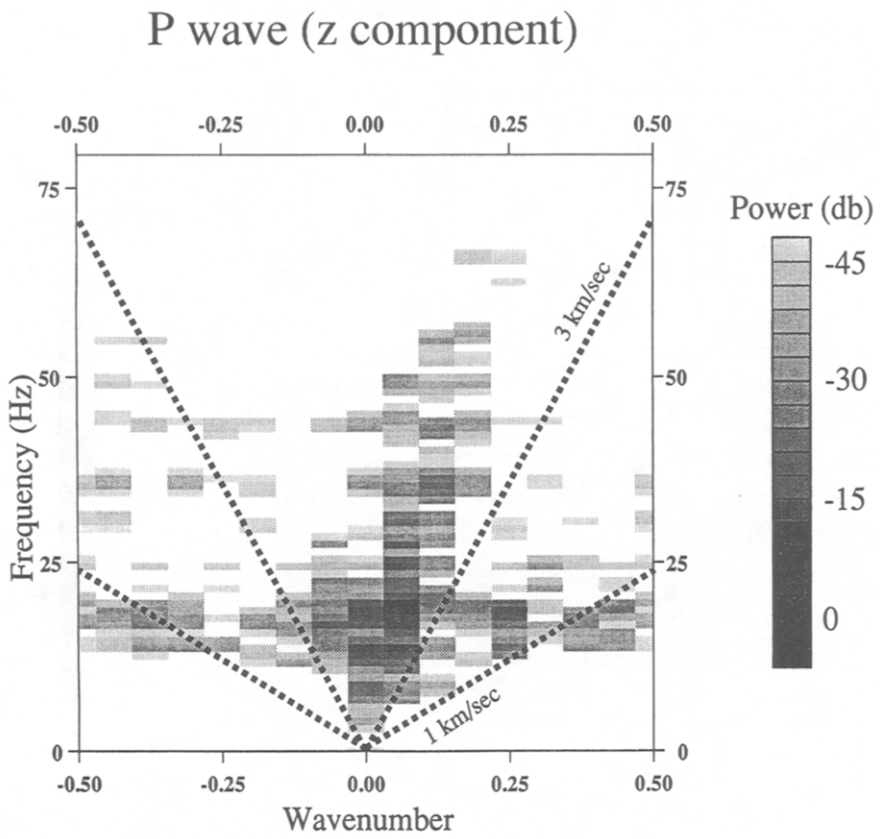


(b)

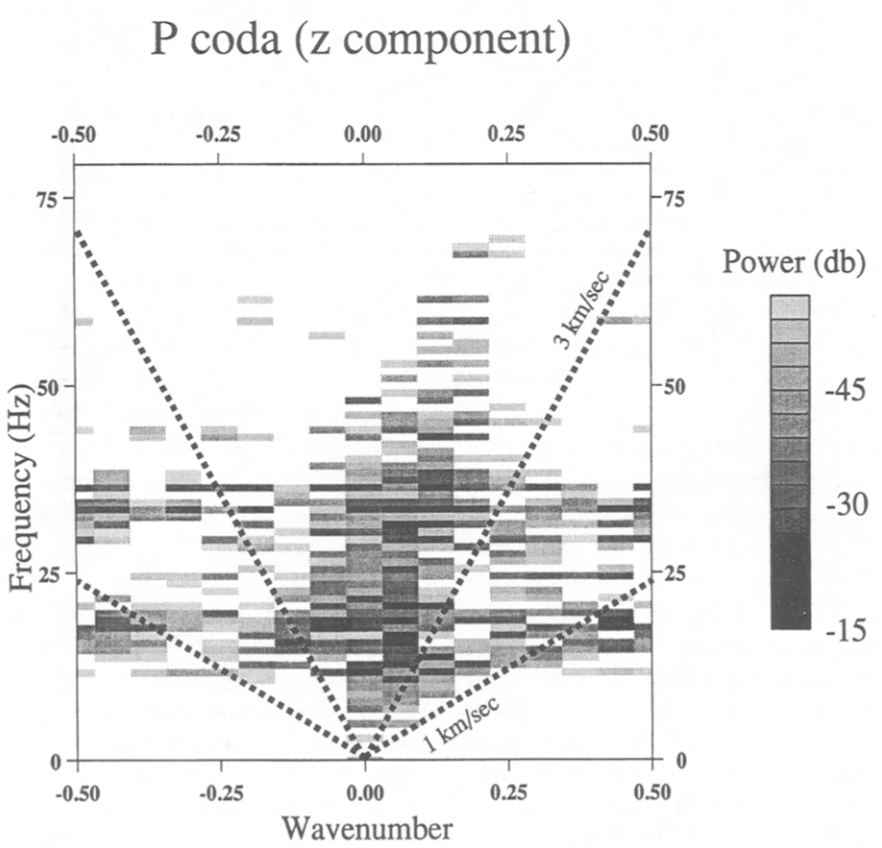


Figure 10. Caption on facing page.

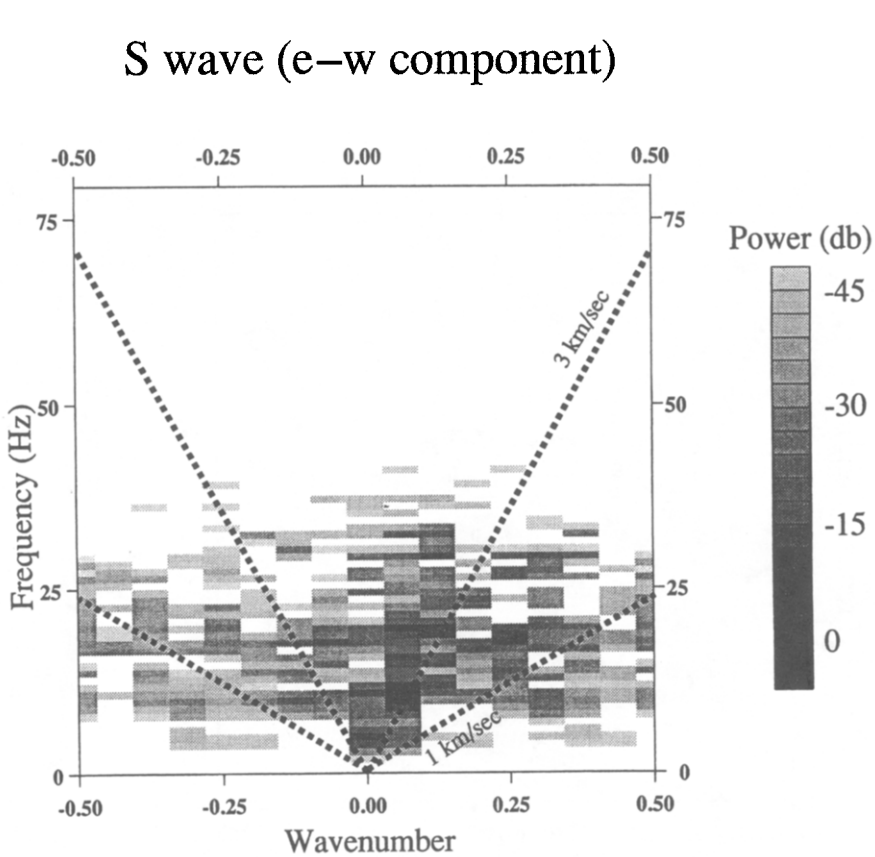


Figure 10. The *f-k* spectra of local earthquake recorded (Fig. 5a) by 13 equally spaced stations along the E–W arm of the array. Part (a) is the *f-k* spectrum for a 1-sec window centered on the *P* wave recorded on the vertical components (marked by the gray shaded box 1 in Fig. 5), (b) is the spectra for a 1-sec window of the *P*-wave coda recorded on the vertical components (marked by the gray shaded box 2 in Fig. 5), and (c) is the *S* wave recorded on the E–W component (waveforms not shown in Fig. 5 for E–W component). In these figures, the wavenumber axis is nondimensional. That is, the nondimensional wavenumber $k' = kx/2\bar{a}$, where $x$ is the sensor spacing (21 m). The spectra are displayed using a gray scale as power in decibels relative to the peak value in all time windows examined. In this case, this is the peak power for the *S* wave on the E–W component (part c). The lines plotted in the figure are reference velocities. That is, these spectra have the property that a signal moving across the array at 3 km/sec would produce a linear spectrum strung out along the 3 km/sec line shown in this figure.

component array vary spatially. This display shows that the first half-cycle of the *P* wave is cleanly seen across the entire array, but after that, the picture quickly breaks down into pseudorandom swirling motion that varies rapidly with position. Hints of the same phenomenon can be seen by simply looking at the conventional display of one event in Figure 8.

5. Frequency-wavenumber spectra and frequency-wavenumber filtering demonstrate quantitatively that the signals we observe are strongly contaminated by seismic waves traveling with low apparent velocities. Because we are observing sources tens of kilometers from the array, body waves from the source should have apparent velocities no lower than the velocity of intact granite (measured here as 5.4 km/sec for *P* waves, so *S* waves should have apparent velocities no lower than about 3.0 km/sec). Yet *f-k* spectra show that significant amounts of the wave field (10 to 30 dB down from direct arrivals) travel at apparent velocities well below the velocity of intact granite.

The most logical model that can explain all these observations is that body waves propagating upward from earthquake sources are scattered in the near surface into body waves trapped in the surface wave guide and high-frequency surface-wave modes associated with the same wave guide. The weathered layer is perfectly suited for this at Pinyon as shown by the observations in 1 and 2 in the previous paragraphs. That is, the weathered layer is highly irregular on scale lengths that are a significant fraction of the wavelength

of incoming body waves. Numerous numerical simulations of this type of geometry (e.g., Hill and Levander, 1984; Gibson and Levander, 1988) indicated that this type of corrugated weathered surface can induce near-surface scattering. These results have serious implications for at least three areas of seismological research presently being actively pursued.

1. There are important practical and basic scientific reasons for improving measurements of source spectra at high frequencies. From a practical side, one of the most thorny technical issues remaining in monitoring underground nuclear testing is discrimination of small, decoupled nuclear tests from natural sources or chemical explosions. A solution to this problem is known but requires the accurate measurement of source spectra at frequencies over a few Hertz (e.g., Evernden *et al.,* 1986; Al-Shukri *et al.,* 1995). This problem with near-surface effects was known from the earliest days of nuclear monitoring, and it is one of the major reasons that large amounts of money are spent on drilling boreholes for monitoring stations. On the other hand, few stations deployed for research purposes can justify the cost of borehole deployments. Hence, fundamental understanding of the types of effects we are observing here are important, and more work will be needed to allow more effective use of high-frequency seismic data.
2. Results from spectral measurements of earthquakes from local and regional networks contain more puzzles than answers, yet characterizing earthquake source spectra is an important goal to improve our understanding of earthquakes. The results presented here demonstrate at least one reason why measurement of source spectral measurements at high frequencies is a difficult problem. The seismograms we recorded at Pinyon are contaminated strongly by near-surface scattering that is brightly colored at high frequencies. There is every reason the same is true of most regional network data.
3. With the emergence of a new generation of seismic instrumentation brought about by the PASSCAL program of the Incorporated Research Institutions for Seismology IRIS), it is now possible to record spatially unaliased records of the seismic wave fields from earthquake sources with an areal array. This experiment is an example. If scaled upward, such experiments have great promise for providing a new view of the Earth's interior by exploiting comparatively "bright" sources produced by earthquakes. The proper deployment strategies for passive arrays of a different scale are poorly known. At the higher frequencies studied here, the effects we have observed here will need to be better understood to properly design seismic arrays.
4. The frequency band of the data we examine here is the same as that utilized in reflection seismology. The sources we observed, however, are orders of magnitude larger, and the wave field is propagating only upward. The same problems we observed here are known to exist in exploration, and the engineering solution is well known. Reflection seismology data collection on land always utilizes geophone subarrays (groups). This article provides an improved fundamental understanding of why geophone subarrays work for improved recording of high-frequency wave fields. Geophone arrays commonly span a scale length of about the size of the grid at the Pinyon array. Combining signals from multiple sensors would smooth out the effects we observe here and significantly improve the coherence between adjacent seismic traces.

This article demonstrates clearly that high-frequency seismograms are seriously distorted by near-surface scattering at this site. The same phenomena almost certainly occurs to some degree at any hard-rock site. We cannot yet, however, easily extrapolate these results to predict the degree of signal-generated noise at a given site. It no doubt depends upon the depth of the weathering and the degree of heterogeneity in the near surface.

## Acknowledgments

This article would not have been possible without the assistance and equipment from the IRIS-PASSCAL Instrument Center at Lamont, the technical staff at IGPP/UCSD including Jeff Babcock, James Battie, Adam Edelman, Paul Henkart, Glen Offield, and Chris Winther. Frank Wyatt provided access to the PFO facility as well as helpful insight about the PFO site characteristics. Joe Fletcher of the U.S. Geological Survey supplied the boreholes with sensors that were critical for the execution of this experiment. This program was funded by the IRIS Eurasian Seismic Studies Program.

## References

Al-Shukri, H. J., G. L. Pavlis, and F. L. Vernon III (1995). Site effect observations from broadband arrays, *Bull. Seism. Soc. Am.* **85,** 1758–1769.

Anderson, P. N. (1993). Animated visualization techniques for three-component seismic array data, *Ph.D. Thesis,* Indiana University, Bloomington, Indiana.

Capon, J., R. J. Greenfield, R. J. Kolker, and R. T. Lacoss (1968). Short-period signal processing results from the large-aperture seismic array, *Geophysics,* **33,** 452–472.

Carpenter, E. W. (1965). An historical review of seismometer array development, *Proc. IEEE* **53,** 1816–1821.

Cummings, D. (1979). Determination of depths to an irregular interface in shallow seismic refraction surveys using a pocket calculator, *Geophysics* **44,** 1987–1998.

Davies, D. (1973). Seismology with large arrays, *Rept. Prog. Phys.* **36,** 1233–1283.

Dibblee, T. W. (1981). Geology of the San Jacinto Mountains and adjacent areas, *Geology of the San Jacinto Mountains,* South Coast Geological Society, 1–47.

Dziewonski, A. M., T. A. Chou, and J. H. Woodhouse (1981). Determination of earthquake source parameters from waveform data for studies of global and regional seismicity, *J. Geophys. Res.* **86,** 2825–2852.

Evernden, J. F., C. B. Archambeau, and E. Cranswick (1986). An evaluation of seismic decoupling and underground nuclear test monitoring using high-frequency seismic data, *Rev. Geophys.* **24,** 143–215.

Fan, G. and T. Wallace (1991). The determination of source parameters for small earthquakes from a single very broadband seismic station, *Geophys. Res. Lett.* **18,** 1385–1388.

Filson, J. (1975). Array seismology, *Ann. Rev. Earth Planet. Sci.* **3,** 157–181.

Fletcher, J. B., T. Fumal, H. Liu, and R. Porcella (1990). Near-surface velocities and attenuation at two bore-holes near Anza, CA, from logging data, *Bull. Seism. Soc. Am.* **80,** 807–831.

Forbes, C. B., R. Obenchain, and R. J. Swain (1965). The LASA sensing system design, installation, and operation, *Proc. IEEE* **53,** 1834–1843.

Gibson, B. S. and A. R. Levander (1988). Modeling and processing of scattered waves in seismic reflection surveys, *Geophysics* **53,** 466–478.

Green, Jr., P. E., R. A. Frosch, and C. A. Romney (1965). Principles of an experimental large aperture seismic array (LASA), *Proc. IEEE* **53,** 1821–1833.

Hagedoorn, J. G. (1959). The plus-minus method of interpreting seismic refraction sections, *Geophys. Prosp.* **7,** 158–181.

Helmberger, D., D. Dreger, R. Stead, and H. Kanamori (1993). Impact of broadband seismology on the understanding of strong motions, *Bull. Seism. Soc. Am.* **83,** 830–850.

Hill, N. R. and A. R. Levander (1984). Resonances of low-velocity layers with lateral variations, *Bull. Seism. Soc. Am.* **74,** 521–537.

Holt, W. E. and T. C. Wallace (1987). A procedure for the joint inversion of regional and teleseismic long-period body waves, *Geophys. Res. Lett.* **14,** 903–906.

King, J. L. and B. E. Tucker (1984). Observed variations of earthquake motion across a sediment-filled valley, *Bull. Seism. Soc. Am.* **74,** 153–165.

Lindseth, R. O. (1982). *Digital Processing of Geophysical Data: A Review,* Soc. Expl. Geophys., Tulsa, Oklahoma.

McLaughin, K. L., L. R. Johnson, and T. V. McEvilly (1983). Two-dimensional array measurements of near-source ground accelerations, *Bull. Seism. Soc. Am.* **73,** 349–375.

Menke, W., L. Shengold, G. Hongsheng, H. Ge, and A. Lerner-Lam (1991). Performance of the short period geophones of the IRIS/PASSCAL array, *Bull. Seism. Soc. Am.* **81,** 232–242.

Owens, T. J., P. N. Anderson, and D. E. McNamara (1991). Data Report for the 1990 Pinyon Flat High Frequency Array Experiment, An IRIS Eurasian Seismic Studies Program Passive Source Experiment, Passcal Data Report 91-002.

Pavlis, G. L. and P. N. Anderson (1990). Visualization techniques for seismic array data, *Geophys.: The Leading Edge of Expl.* **9,** 26–29.

Repin, D. G. and G. L. Pavlis (1997). Interactive three-dimensional visualization of seismic array data, *Comput. Geosci.* **23,** 1079–1092.

Song, X. and D. V. Helmberger (1992). Velocity structure near the inner core boundary from waveform modeling, *J. Geophys. Res. (B),* **97,** 6573–6586.

Thomson, D. J. (1982). Spectrum estimation and harmonic analysis, *Proc. IEEE* **70,** 1055–1096.

Vernon, F. L., J. Fletcher, L. Carroll, A. Chave, and E. Sembera (1991). Coherence of seismic body waves from local events as measured by a small-aperture array, *J. Geophys. Res.* **96,** 11981–11996.

Wyatt, F. (1982). Displacement of surface monuments: horizontal motion, *J. Geophys. Res.* **87,** 979–989.

Wyatt, F. (1989). Displacement of surface monuments: vertical motion, *J. Geophys. Res. (B)* **94,** 1655–1664.

Institute of Geophysics and Planetary Physics
University of California at San Diego
La Jolla, California 92093
(F. V.)

Department of Geological Sciences
Indiana University
1005 10th St.
Bloomington, Indiana 47405
(G. P.)

Department of Geological Sciences
The University of South Carolina
Columbia, South Carolina 29208
(T. O.)

University of Alaska, Fairbanks
903 Koyukuk Dr., POB 757320
Fairbanks, Alaska 99775-7320
(D. M.)

BP Exploration Inc.
8332 Leamont Dr.
Houston, Texas 77072
(P. A.)

Manuscript received 16 May 1995.